



**Lattice Expansion and Ligand Twist during CO<sub>2</sub> Adsorption  
in Flexible Cu Bipyridine Metal-Organic Frameworks**

Journal:	<i>Journal of Materials Chemistry A</i>
Manuscript ID	TA-ART-03-2020-003298.R2
Article Type:	Paper
Date Submitted by the Author:	18-Aug-2020
Complete List of Authors:	Marks, Samuel; University of Wisconsin Madison, Department of Materials Science and Engineering; University of Wisconsin Riascos-Rodriguez, Karina; University of Puerto Rico - Mayaguez, Department of Chemical Engineering Arrieta-Perez, Rodinson; Recinto Universitario de Mayaguez Universidad de Puerto Rico, Chemical Engineering Yakovenko, Andrey; Argonne National Laboratory, X-ray Science Division Exley, Jason; Micromeritics Instrument Corp Evans, Paul; University of Wisconsin Madison, Department of Materials Science and Engineering Hernandez-Maldonado, Arturo; University of Puerto Rico Mayaguez, Department of Chemical Engineering

## Lattice Expansion and Ligand Twist during CO<sub>2</sub> Adsorption in Flexible Cu Bipyridine Metal-Organic Frameworks

Samuel D. Marks,<sup>1\*</sup> Karina Riascos-Rodriguez,<sup>2</sup> Rodinson R. Arrieta-Pérez,<sup>2</sup> Andrey A. Yakovenko,<sup>3</sup> Jason Exley,<sup>4</sup> Paul G. Evans,<sup>1</sup> and Arturo J. Hernández-Maldonado<sup>2</sup>

<sup>1</sup> *Department of Materials Science and Engineering, University of Wisconsin, Madison, WI 53706*

<sup>2</sup> *Department of Chemical Engineering, University of Puerto Rico, Mayaguez, PR 00681*

<sup>3</sup> *Advanced Photon Source, Argonne National Laboratory, Argonne, Illinois 60439*

<sup>4</sup> *Micromeritics Instrument Corporation, Norcross, GA 30093*

### *Abstract*

Flexible metal-organic frameworks (MOFs) can show exceptional selectivity and capacity for adsorption of CO<sub>2</sub>. The incorporation of CO<sub>2</sub> into flexible MOFs that have Cu<sup>2+</sup> coordination centers and organic pillar ligands is accompanied by a distortion of the framework lattice arising from chemical interactions between these components and CO<sub>2</sub> molecules. CO<sub>2</sub> adsorption yields a reproducible lattice expansion that is enabled by the rotation of the pillar ligands. The structures of Cu<sub>2</sub>(pzdc)<sub>2</sub>(bpy) and Cu<sub>2</sub>(pzdc)<sub>2</sub>(bpe), CPL-2 and CPL-5, were evaluated using *in situ* synchrotron x-ray powder diffraction at room temperature at CO<sub>2</sub> gas pressures up to 50 atm. The structural parameters exhibit hysteresis between pressurization and depressurization. The pore volume within CPL-2 and CPL-5 increases at elevated CO<sub>2</sub> pressure due to a combination of the pillar ligand rotation and the overall expansion of the lattice. Volumetric CO<sub>2</sub> adsorption measurements up to 50 atm reveal adsorption behavior consistent with the structural results, including a rapid uptake of CO<sub>2</sub> at low pressure, saturation above 20 atm, and hysteresis evident as a retention of CO<sub>2</sub> during depressurization. A significantly greater CO<sub>2</sub> uptake is observed in CPL-5 in comparison with predictions based on CO<sub>2</sub> pressure-induced expansion of the pore

volume available for adsorption, indicating that the flexibility of the CPL structures is a key factor in enhancing adsorption capacity.

## 1. Introduction

The separation of carbon dioxide (CO<sub>2</sub>) from gas mixtures is a key step in technological processes and presents fundamental scientific challenges in molecular design and in understanding gas-solid interactions. Post-combustion CO<sub>2</sub> capture is typically achieved using absorption, adsorption, or membrane technologies that rely on physical or chemical interactions between CO<sub>2</sub> and a sorbent to selectively remove CO<sub>2</sub> from gas mixtures.<sup>1-3</sup> Cyclic separation processes often employ porous materials such as silica gels, aluminosilicate zeolites and activated carbons that can be regenerated once the working capacity of the material is achieved.<sup>4</sup> The performance of these materials in CO<sub>2</sub>-capture applications is limited by insufficient CO<sub>2</sub> capacity and selectivity, high temperature required for regeneration, and the production of environmentally harmful by-products.<sup>5,6</sup> The limitations of present CO<sub>2</sub> capture technologies, together with the need to reduce the production of atmospheric CO<sub>2</sub>, have motivated research efforts into new CO<sub>2</sub> capture materials.

Metal-organic frameworks (MOFs) are crystalline organometallic complexes incorporating metal-ion coordination centers and organic pillar ligands.<sup>7</sup> The composition and structure of MOFs can be specifically selected to provide CO<sub>2</sub> capture materials with promising properties. Computational studies indicate that the gas adsorption capacity and selectivity can be predicted based on compositional and structural descriptors.<sup>8</sup> Key structural parameters such as porosity, crystallinity, and internal surface area of MOFs can be controlled through the selection of the metal ion coordination center or functionalization of the ligands.<sup>9-12</sup> MOFs can have crystal lattices that can be distorted in response to external stimuli such as the addition of guest molecules

within the pores of the structure.<sup>13-15</sup> The degree to which the structure distorts in response to external stimuli depends on the chemical design of the MOF, including the coordination of the N donor ligand and metal nodes. The magnitude of the variations in the unit cell dimensions and molecular configuration also depend on interactions between the adsorbed gas molecules and the MOF crystal structure.<sup>16-20</sup> The results of these previous studies suggest that optimized MOF-based CO<sub>2</sub>-separation materials may have the potential to exhibit simultaneously high selectivity and capacity at room temperature while requiring lower energy inputs for regeneration than in other approaches.

A large class of MOFs termed porous coordination polymers with pillared layer structures (CPL) includes compounds in which ligands are coordinated to Cu<sup>2+</sup> nodes to form a manifold-like framework with one-dimensional galleries or pore channels.<sup>21, 22</sup> We focus here on the CO<sub>2</sub> adsorption-induced structural changes in two CPL MOFs that show high adsorption capacity and selectivity for CO<sub>2</sub>: (i) Cu<sub>2</sub>(pzdc)<sub>2</sub>(bpy) (CPL-2) and (ii) Cu<sub>2</sub>(pzdc)<sub>2</sub>(bpe) (CPL-5). Here, *pzdc*, *bpy* and *bpe* denote pyrazine 2,3-dicarboxylate, 4,4'-bipyridine, and 1,2-di-(4-pyridyl)ethylene ligands, respectively.<sup>22, 23</sup> These CPL compounds incorporate two-dimensional neutral layers of pyrazine-2,3-dicarboxylate (*pzdc*) units bonded to copper (Cu<sup>2+</sup>) nodes and linked together with organic pillar ligands. Both CPLs exhibit selective adsorption of CO<sub>2</sub> in the presence of mixtures containing N<sub>2</sub>, O<sub>2</sub>, and CH<sub>4</sub>.<sup>23-25</sup> There is extensive insight available into the structure, thermodynamics, chemical modification, and gas-adsorption behavior of CPL compounds. This high level of background information makes the CPL compounds an excellent model system in which to explore subtle structural phenomena that, in-turn, can provide insight across the wider scope of MOFs.

The synthesis of CPL-2 and CPL-5 and characterization of their structural and chemical properties have been extensively described, making them excellent candidates for detailed *in situ* structural study.<sup>23, 26, 27</sup> The unit cells of CPL-2 (space group  $P2_1/c$ ,  $a = 4.712\text{\AA}$ ,  $b = 27.833\text{\AA}$ ,  $c = 10.888\text{\AA}$ ,  $\beta = 96.0102^\circ$ ) and CPL-5 (space group  $P2_1/c$ ,  $a = 4.711\text{\AA}$ ,  $b = 31.858\text{\AA}$ ,  $c = 11.002\text{\AA}$ ,  $\beta = 96.008^\circ$ ) crystals under ambient conditions are shown in Fig. 1.<sup>†</sup>

In comparison with CPL-2, CPL-5 has a larger pore gallery volume as a result of its additional ethene spacer located between pyridines of the pillar ligand. The *bpe* CPL-5 pillar is 25% longer than the *bpy* ligand in CPL-2, resulting in a 16% larger unit cell volume for CPL-5 that matches the pore volume determined computationally.<sup>28</sup>

Both CPL-2 and CPL-5 exhibit selectivity and adsorption for  $\text{CO}_2$  due to interaction between the electric field gradient generated by the internal surface of the CPL framework and the permanent electric quadrupole moment of  $\text{CO}_2$ .<sup>20, 24</sup> During the adsorption process,  $\text{CO}_2$  molecules move through the channels of CPL-2 and CPL-5 shown in Fig. 1 and reach interaction sites on the

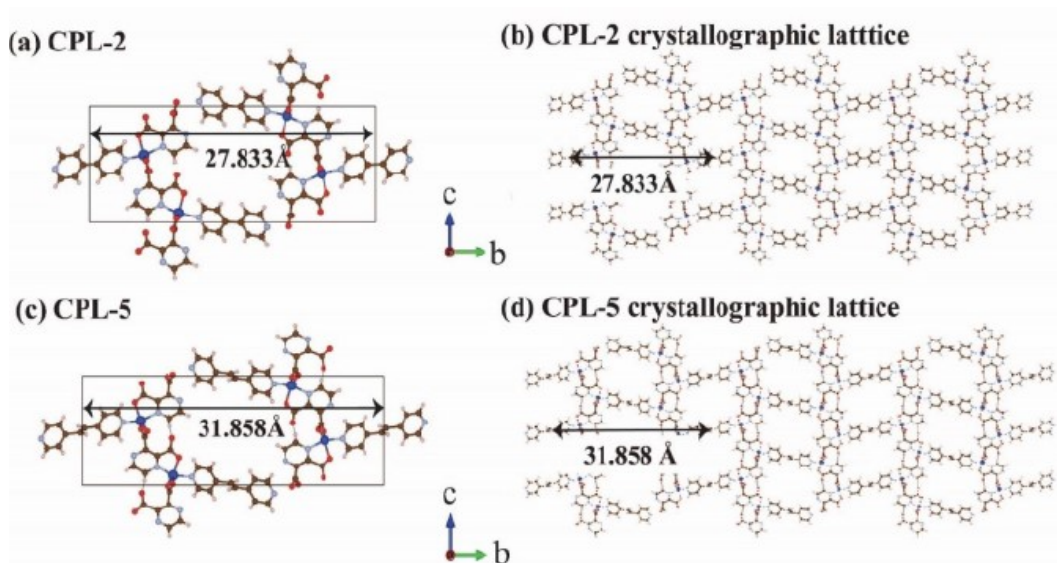


Figure 1. (a) Single unit cell and (b) crystallographic lattice of CPL-2. (c) Single unit cell and (d) crystallographic lattice of CPL-5. The dimension along the *b* axis is labeled for each unit cell.

surfaces of the pore structure.<sup>10</sup> The crystal structures of the CPL framework shrink as the gas molecules desorb when the CO<sub>2</sub> pressure is reduced.<sup>21, 29</sup> Significant progress has been made in characterizing and modeling the capacity and selectivity for CO<sub>2</sub> adsorption in CPLs.<sup>24, 25, 27, 28</sup> The solvent accessible volume can be predicted from the volume of the porous channels, which depends on the distance between the N atoms of each bidentate pillar ligand.<sup>22</sup> Several basic aspects of the response of the lattice to CO<sub>2</sub> adsorption are also clear. Previous studies of CPL-2 in CO<sub>2</sub> gas atmospheres up to 7 atm show that the (020) interplanar spacing changes differ during adsorption and desorption, exhibiting hysteresis as a function of the gas pressure.<sup>33</sup>

This manuscript reports insight into the structural aspects of CO<sub>2</sub> adsorption derived from synchrotron powder X-ray diffraction experiments probing CPL-2 and CPL-5 at CO<sub>2</sub> pressures up to 50 atm. The changes in the lattice parameters in CPL-2 and CPL-5 reveal an overall lattice expansion driven by CO<sub>2</sub> adsorption. Analysis using Rietveld refinement shows that there is an atomic rearrangement within the CPL unit cell in which the organic ligands twist about their major axes. A complementary series of control experiments was conducted using high pressure N<sub>2</sub> gas, for which CPL-2 and CPL-5 have negligible adsorption.<sup>23, 25</sup> Volumetric adsorption-desorption isotherms in the same pressure regime were also gathered to provide insight into the CO<sub>2</sub> adsorption-driven mechanism for the distortion of the CPL-2 and CPL-5 crystal structures.

## 2. Experimental Conditions

Gas pressures throughout the manuscript are reported as gauge pressures such that 0 atm-gauge CO<sub>2</sub> corresponds to a total pressure of 1 atm of CO<sub>2</sub> and similar considerations apply to N<sub>2</sub> and He pressures. Further details are presented in the Experimental section.

### 2.1 Activation and Pressurization Conditions.

The *in situ* CO<sub>2</sub> adsorption diffraction study powder diffraction study consisted of a series of structural measurements conducted at room temperature as a function of the gas environment and pressure. The as-synthesized CPL powder was activated by heating to 100 °C in He at 0 atm for 60 min to remove trapped solvent molecules and other impurities. Among the X-ray diffraction signatures of the activation of both compounds were shifts of the 020 X-ray reflections to higher  $2\theta$  angle and increases in the intensity of the 020 reflection. The time evolution of the diffracted intensity for CPL-2 and CPL-5 during the activation process are shown in Figs. 2(a) and 2(b).

The gas environment was switched to CO<sub>2</sub> after activation and the structure was studied at 0 atm CO<sub>2</sub>. In the studies at elevated pressure the CO<sub>2</sub> pressure was increased in discrete steps from 0 atm to 50 atm, followed by a return to 0 atm in similar steps. Diffraction patterns were

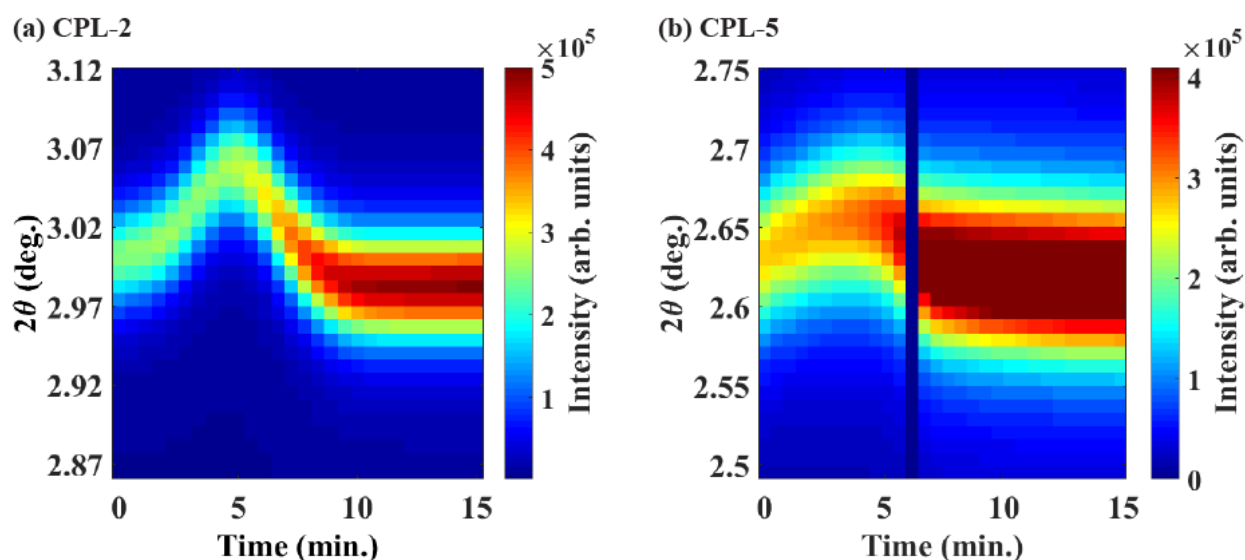


Figure 2. Intensity of the 020 reflection as a function of time and  $2\theta$  angle for (a) CPL-2 and (b) CPL-5 during the activation procedure. The column of zero value pixels at 6 min in (b) indicates a period of the experiment in which data was not collected due to an experimental fault.

collected from CPL-5 at the following CO<sub>2</sub> pressures: 0 atm, 4, 7, 10, 15, 20, 25, 30, 35, 40, 45, 50. The same CO<sub>2</sub> pressures were used in the CPL-2 study, with one additional point at 1 atm.

The total period of each pressure cycle was 4.5 h. Figures 3(a) and 3(b) show the distribution of

diffracted intensity and angle of the 020 reflection during CO<sub>2</sub> adsorption and desorption and after the activation process at 0 atm He before exposure to CO<sub>2</sub>. The 2 $\theta$  angle of the 020 reflection

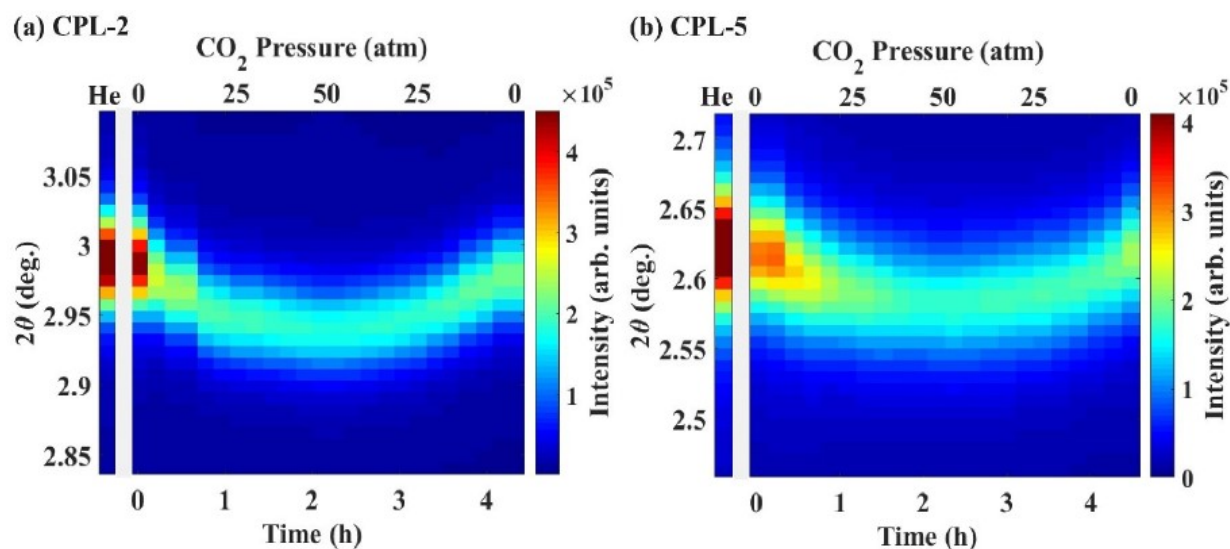


Figure 3. Intensity of the 020 reflection as a function of time and 2 $\theta$  angle for (a) CPL-2 and (b) CPL-5 during a complete cycle consisting of activation, pressurization, and depressurization. The first vertical column of each plot shows the angular dependence of the intensity of the 020 reflection at 0 atm He after activation.

decreased during the increase in CO<sub>2</sub> pressure and subsequently returned towards its initial value during depressurization. The integrated intensity of the 020 reflection decreased during pressurization to 50 atm and partially recovered as the pressure returned to 0 atm. The structural changes that led to the observed angular shift and intensity variation are discussed in detail below.

The adsorption isotherm experiments were conducted using a similar sequence of gas pressure steps. Each CPL powder was activated prior to adsorption isotherm experiments by heating to 100 °C in vacuum for a minimum of 4 h and were cooled to 25 °C for the adsorption measurements. A blank run using an empty sample cell was conducted prior to the acquisition of each adsorption isotherm using the same analysis gas composition, temperature, and pressure. The blank run data were subtracted from the sample analysis data to correct for small errors resulting from the increasing density of CO<sub>2</sub> at elevated pressures.<sup>36</sup>

The isotherms in Fig. 4 show the total adsorbed amount of CO<sub>2</sub> per gram of CPL-2 and CPL-5 as a function of CO<sub>2</sub> pressure up to 50 atm. The high-pressure volumetric adsorption study reveals a considerable difference in the CO<sub>2</sub> uptake of CPL-2 and CPL-5. The CO<sub>2</sub> loadings observed at 50 atm differ by more than 50%, with CPL-5 and CPL-2 adsorbing 5.2 mmol g<sup>-1</sup> and 3.25 mmol g<sup>-1</sup>, respectively. Based on the difference in the pore gallery volume between CPL-2 and CPL-5, we expect CPL-5 to have a 16% higher adsorbed amount. The discrepancy between the predicted and observed

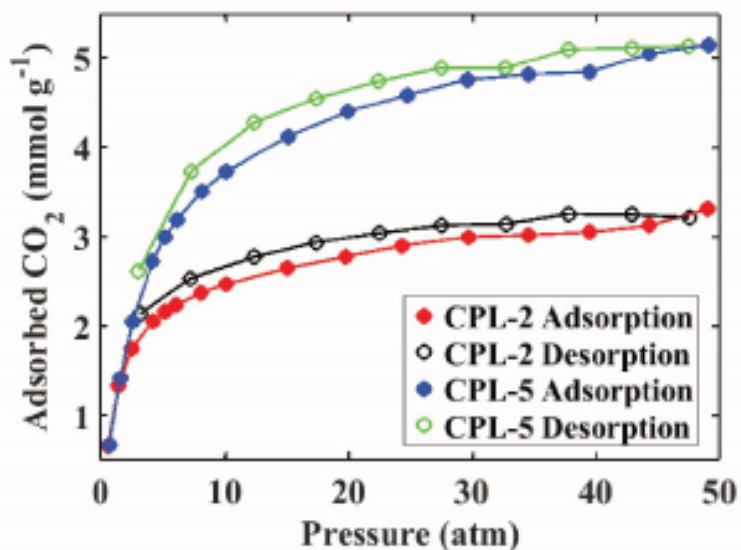


Figure 4. Adsorption and desorption isotherms for CPL-2 and CPL-5 for CO<sub>2</sub> pressures up to 50 atm.

adsorbed amount indicates differences in the structural responses of CPL-2 and CPL-5 to high-pressure CO<sub>2</sub> gas environments. The convergence of the adsorption isotherms as zero loading is approached indicates CPL-2 and CPL-5 are fully regenerable, consistent with previous studies.<sup>24, 27, 29</sup>

The interactions between CO<sub>2</sub> and the CPL materials quantified by analyzing the adsorption and desorption legs of the data shown in Figure 5 using equations 3-5 (see Experimental section). The resulting Dubinin-Astakhov isotherm model parameters and heat profiles are shown in Table 1 and Figure 5, respectively. The heat profiles at near zero CO<sub>2</sub> pressure indicated that CO<sub>2</sub> interactions with CPL-2 that are much stronger than those of CPL-5; this also reflected in the energy parameter ( $\beta$ DAE) values. It appears that the interaction of CO<sub>2</sub> with bpy ligands or the effective surface environment that these create is greater compared to bpe.

**Table 1. Dubinin-Astakhov (DA) isotherm model parameters from CO<sub>2</sub> adsorption/desorption isotherms at 25 °C.**

Adsorbent		DA Isotherm Parameters			
		$q_0$ (mmol/g)	$\beta_{DA}E$ (kJ/mol)	$n$ (-)	Std. Dev.*
CPL-2	adsorption	3.123	9.934	1.988	± 0.044
	desorption		12.451	1.598	± 0.049
CPL-5	adsorption	4.989	8.297	2.099	± 0.030
	desorption		9.181	2.032	± 0.045

\* Standard deviation calculated based on residuals between the observed and calculated equilibrium loading amounts for the complete pressure range.

## 2.2 Structure Refinement

The details of the Rietveld refinement procedure are discussed in the Experimental section below. Table 2 lists the experimental conditions of the powder diffraction data acquisition, the refinement parameters of the Rietveld refinement, and the chemical and structural parameters of activated CPL-2

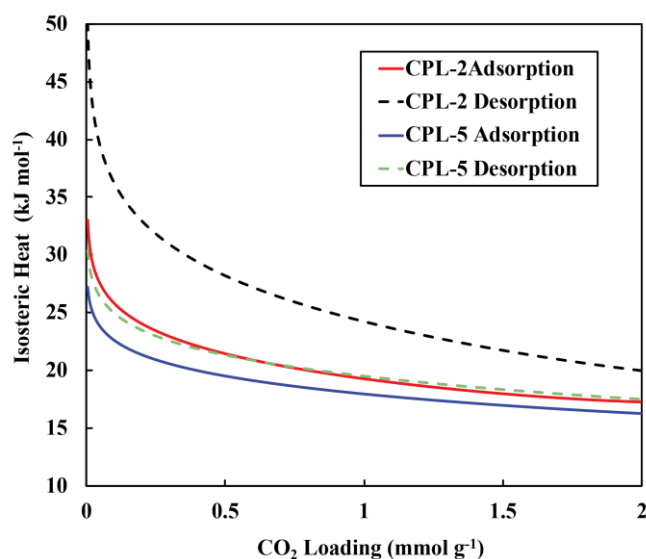


Figure 5. CO<sub>2</sub> heat of adsorption and desorption profiles for CPL-2 and CPL-5.

and CPL-5 at ambient temperature and 0 atm in He. The chemical composition, unit cell geometry, and crystal symmetry data listed in Table 2 were obtained from a crystallographic database.<sup>†</sup>

The structural models derived from CPL-2 and CPL-5 powder diffraction patterns were refined using a parametric fitting strategy employing an initial structure model to which small

**Table 2: Data Collection and Crystallographic Data for CPL-2 and CPL-5 in the activated state at atmospheric pressure.**

**Data Collection**

X-ray source	Station 17-BM, Advanced Photon Source
Wavelength (Å)	0.79768
Step (deg.)	0.008
2θ range (deg)	1-22

<b>Phase</b>	<b>CPL-2</b>	<b>CPL-5</b>	<b>CPL-2*</b>	<b>CPL-5*</b>
Formula	C <sub>11</sub> H <sub>6</sub> CuN <sub>3</sub> O <sub>4</sub>	C <sub>12</sub> H <sub>7</sub> CuN <sub>3</sub> O <sub>4</sub>		
Molecular mass (g/mol)	308.74	321.76		
Density (g cm <sup>-3</sup> )	1.440	1.272		
T (K)	298	298		
Crystal system	monoclinic	monoclinic		
Space group	P2 <sub>1</sub> /c	P2 <sub>1</sub> /c		
<i>a</i> (Å)	4.7160(3)	4.7109(5)	4.6933(3)	4.7592(9)
<i>b</i> (Å)	27.833(2)	31.858(3)	27.877(1)	32.0854(3)
<i>c</i> (Å)	10.8881(7)	11.002(1)	10.915(60)	11.0366(3)
<i>β</i> (deg.)	96.103(7)	96.008(3)	96.15(1)	96.18(7)
Volume (Å <sup>3</sup> )	1429.2	1651.2	1419.93(8)	1675.51(8)

\*Values obtained for activated CPL-2 and CPL-5 in He.

changes were made at each CO<sub>2</sub> pressure step. Figure 6 shows experimental powder diffraction patterns, diffraction patterns calculated from the refined structure, and the difference between the experimental and calculated patterns for CPL-2 and CPL-5 acquired at 0 atm He immediately after activation. The background intensity distribution subtracted from each diffraction pattern is also plotted in Fig. 6. The profile of the residual indicates that there are differences between the predicted and observed intensity distributions originating from small discrepancies in peak widths, fractional atomic coordinates of atoms within the unit cell, and missing or spurious peaks.

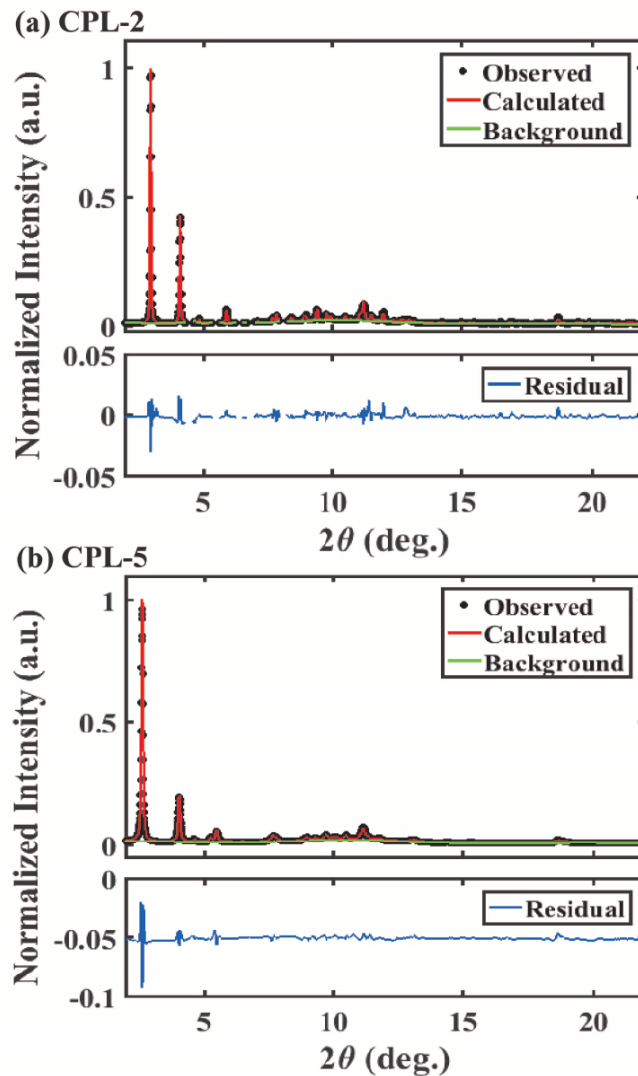


Figure 6. Observed and calculated diffraction patterns obtained using the structure determined from Rietveld analysis for (a) CPL-2 and (b) CPL-5 in He after activation. The difference between observed and calculated patterns is shown in the residual plots. Units of the residual are the same as the diffraction pattern plot.

### 3. Results

#### 3.1 Variation of the CPL-2 Lattice Parameters as a Function of CO<sub>2</sub> Pressure

The pressure-induced changes in the lattice parameters  $a$ ,  $b$ ,  $c$ , and  $\beta$  of CPL-2 during CO<sub>2</sub> adsorption and desorption are shown in Fig. 7. The largest variations of the CPL-2 structure occurred in the parameters  $b$ ,  $c$ , and  $\beta$ . The value of  $b$  increased with increasing CO<sub>2</sub> pressure, from

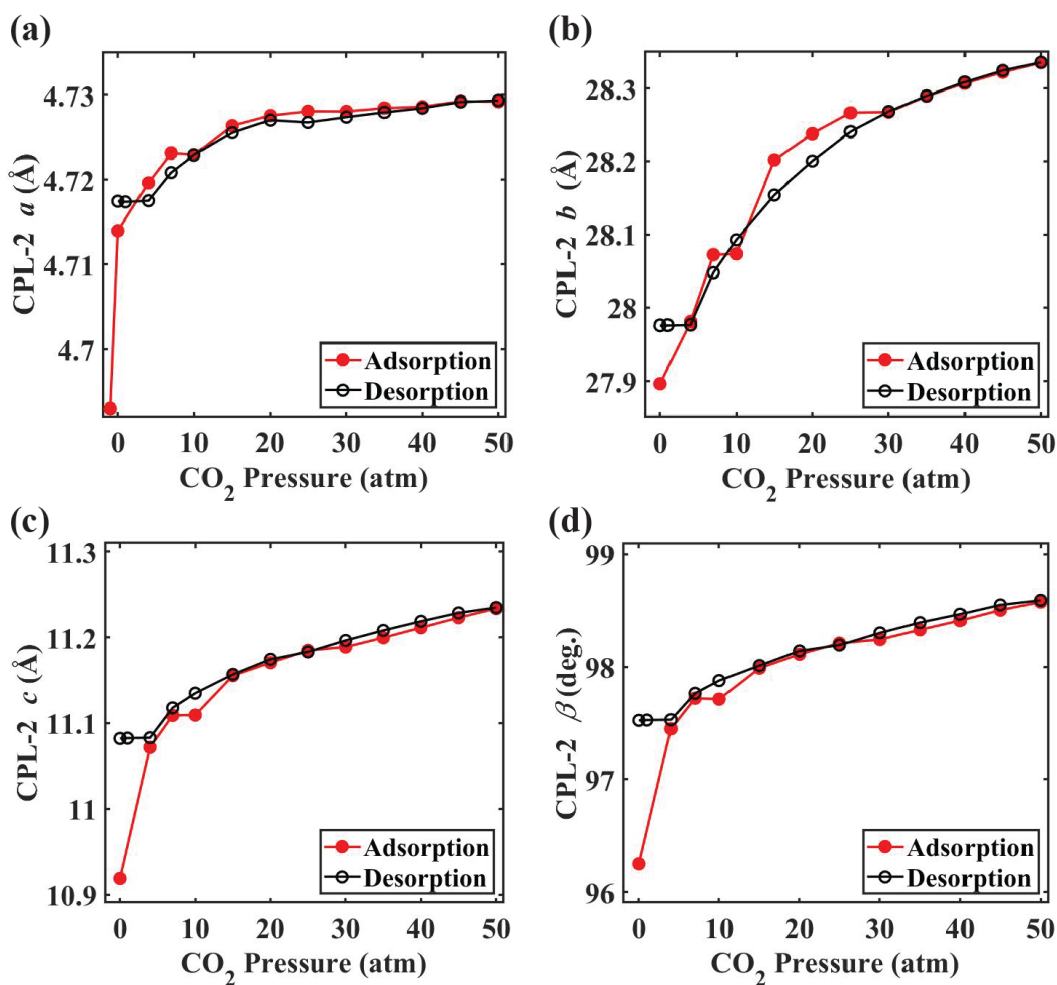


Figure 7. (a)  $a$ , (b)  $b$ , (c)  $c$ , and (d)  $\beta$  lattice parameters of CPL-2 as a function of CO<sub>2</sub> pressure during CO<sub>2</sub> adsorption and desorption. The first point of the adsorption process represents the activated structure in 0 atm He.

27.95 Å at 0 atm to 28.34 Å at 50 atm, corresponding to an expansion of 1.4%. The value of  $b$  decreased to 27.98 Å after the CO<sub>2</sub> pressure was returned to 0 atm. The lattice parameter  $c$  is 10.95

Å in the activated structure at 0 atm He and increased by 2.6% to 11.23 Å at 50 atm CO<sub>2</sub>. The value of  $c$  decreased to 11.08 Å when the pressure was released. The activated CPL-2 structure had  $\beta = 96.2^\circ$ . During the adsorption/desorption cycle,  $\beta$  was  $98.6^\circ$  at 50 atm of CO<sub>2</sub> and was  $97.3^\circ$  at 0 atm CO<sub>2</sub> after the pressure was decreased. The changes in the lattice parameter  $a$  were approximately an order of magnitude smaller than the changes in  $b$  and  $c$ . The small change in  $a$  is discussed in more detail in the discussion section below. The values of  $a$  increased by 0.02 Å from its initial value of 4.7 Å at low CO<sub>2</sub> pressures up to 5 atm and then a further increase by less than 0.01 Å at up to 50 atm.

### 3.2 Variation of the CPL-5 Lattice Parameters as a Function of CO<sub>2</sub> Pressure

The changes in the unit cell volume and lattice parameters of CPL-5 are shown in Fig. 8. The lattice parameters  $b$  and  $c$  of the activated CPL-5 structure at 0 atm He were 32.09 Å and 11.04 Å, respectively. During CO<sub>2</sub> adsorption at pressures up to 50 atm,  $b$  increased to 32.59 Å (a change of 1.6 %) and  $c$  increased to 11.28 Å (a change of 2.2 %). The value of  $\beta$  started at  $96.29^\circ$  after activation, increased to  $97.86^\circ$  during the adsorption/desorption cycle, and returned to the initial magnitude after the CO<sub>2</sub> is released. As was the case for CPL-2, the changes in the  $a$  lattice parameter were smaller by more than an order of magnitude than changes in  $b$  and  $c$ . The lattice parameter  $a$  had a non-monotonic change as function of CO<sub>2</sub> pressure, increasing from 4.76 Å to 4.78 Å at 50 atm during pressurization, then returning to 4.76 Å after depressurization. After the CO<sub>2</sub> pressure is released,  $a$ ,  $b$ , and  $c$  returned to their initial values within experimental error.

The lattice distortion trends in CPL-5 show a small degree of hysteresis in the adsorption-desorption loops. The hysteresis is most evident in  $b$ ,  $c$ , and  $\beta$ , which show pronounced path

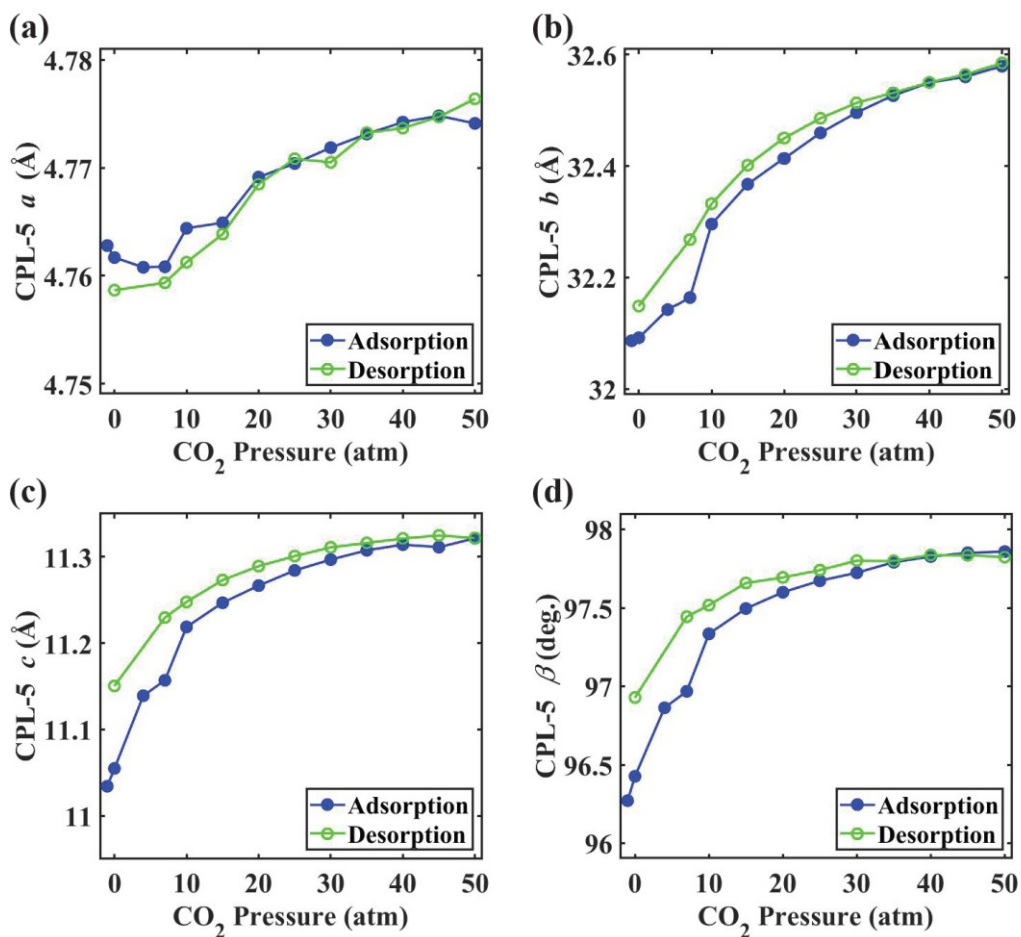


Figure 8. (a)  $a$ , (b)  $b$ , (c)  $c$ , and (d)  $\beta$  lattice parameters of CPL-5 as a function of CO<sub>2</sub> pressure during CO<sub>2</sub> adsorption and desorption. The first point of the adsorption process represents the activated structure in 0 atm He.

differences from adsorption to desorption. The origin of the observed hysteresis is discussed below.

### 3.3 Residual Electron Density: Active Sites on CPL Frameworks for CO<sub>2</sub> Adsorption

The weighted profile residual (Rwp) from the Rietveld analysis is plotted in Fig. 9 as a function of CO<sub>2</sub> pressure. The values of Rwp are determined from the observed and calculated intensities of the Bragg reflections captured in the powder diffraction profiles using the formula

described in the experimental section. The values of Rwp increase from 11.9 and 9.3 after activation in 0 atm He to 18.5 and 17.2 for CPL-2 and CPL-5, respectively. For a structure refinement in which there is no deviation between the observed and measured structure factors, Rwp goes to zero. The relatively high Rwp values reported here likely originate from the inclusion of disordered CO<sub>2</sub> molecules during the sorption experiments. The trend in Rwp obtained from refinements of the CPL structures during adsorption exhibit abrupt increases at CO<sub>2</sub> pressures of 2 atm for CPL-2, and 10 atm for CPL-5.

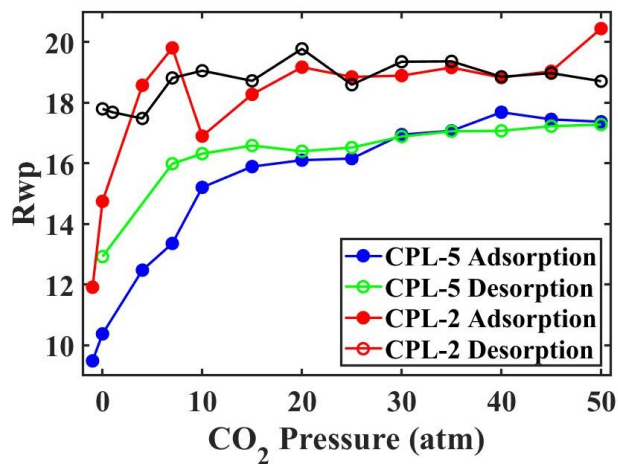


Figure 9. Weighted profile residuals (Rwp) from the Rietveld refinements as a function of CO<sub>2</sub> pressure for CPL-2 (red) and CPL-5 (blue).

We hypothesize that the high values of the refinement residuals at CO<sub>2</sub> pressures between 2 and 50 atm may result from the addition of CO<sub>2</sub> in the pore galleries. The inclusion of the disordered gas molecules in the structural model of CPL lattices complicates the refinement since the precise fractional atomic coordinates of disordered CO<sub>2</sub> cannot be fixed, even for the confined volume of a prospective adsorbed phase. Therefore, CO<sub>2</sub> molecules cannot be simply added to the CPL unit cell as a modification to the crystalline phase. However, the electronic contribution of the CO<sub>2</sub> to the overall charge scattering is crucial to identifying the positions of the CO<sub>2</sub> molecules within the CPL unit cell.

The structure factor for a reflection with indices  $hkl$  is

$$F_{hkl} = \sum_n f_n e^{2\pi(hx+ky+lz)} \quad \text{Equation 1}$$

where  $f_n$  is the atomic form factor of the atom with index  $n$ . The modulus of the structure factor

$F_{hkl}$  is  $|F_{obs}|$ , determined from the peak intensity  $I_{hkl}$  using

$$I_{hkl} = \Phi_0 r_o^2 P |F_{hkl}|^2 N \frac{\lambda}{V_{cell}} \frac{1}{\sin 2\theta} \quad \text{Equation 2}$$

where  $\Phi_0$  is the incident photon flux,  $r_o$  is the Thomson scattering length,  $P$  is the polarization factor for horizontally polarized incident synchrotron X-ray radiation,  $N$  is the number of unit cells, and  $\lambda$  is the wavelength of the incident X-rays. The residual electron density  $\rho(\mathbf{X})$  at fractional position  $\mathbf{X}$  within the unit cell is then

$$\rho(\mathbf{X}) = \frac{1}{V_{cell}} \sum_{h,k,l} (2 * (|F_{obs}| - |F_{calc}|)) e^{2\pi i \mathbf{X} \cdot (h,k,l)}. \quad \text{Equation 3}$$

Here,  $|F_{calc}|$  is the calculated structure factor and  $|F_{obs}| - |F_{calc}|$  is determined for all recorded reflections.

Insight into the possible positions of the CO<sub>2</sub> molecules within the unit cell can be derived from the residual electron density. A series of Fourier difference maps were calculated from the refined CPL crystal structures to show the residual electron density for several key CO<sub>2</sub> pressure

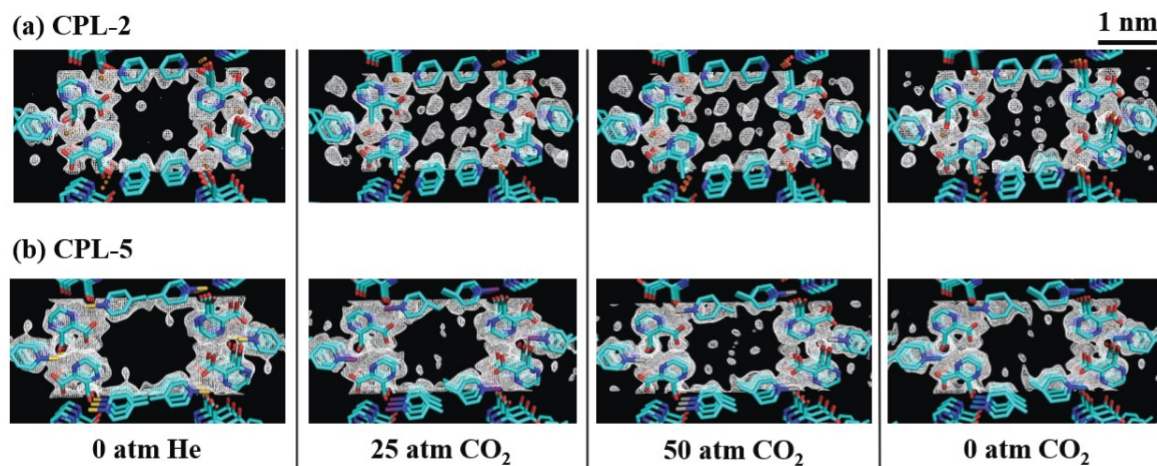


Figure 10. Fourier difference maps of residual electron density inside the pore galleries of (a) CPL-2 and (b) CPL-5.

steps of the adsorption cycle. Mesh contours in Fig. 10 show the surface along which an electron density of 0.5 electrons  $\text{\AA}^{-3}$  is distributed. This value is selected to be slightly greater than the

average electronic density of the observed adsorption  $\text{CO}_2$  capacity, three  $\text{CO}_2$  molecules, distributed over the free volume accessible for adsorption as defined enclosed by the Connolly surface, in this case 132 electrons distributed in a free volume of  $400 \text{ \AA}^3$ .<sup>31</sup> The Fourier maps exhibit features arising from the contribution of adsorbed  $\text{CO}_2$  to the residual electron density distribution. The residual electron density distributed in the interior of the pore galleries is consistent with the presence of  $\text{CO}_2$  in the porous structure of the CPLs. In addition to the illustrating the location of the residual electron density, Fig. 10 also illustrates the variation of the pyridyl ring orientation, which is apparent in change in the angles of the pillars at the top and bottom of each panel.

#### 4. Discussion

The evolution of the lattice parameters during  $\text{CO}_2$  adsorption and desorption shows that CPL-2 and CPL-5 exhibit a structural response to  $\text{CO}_2$  that varies concomitantly with the equilibrium  $\text{CO}_2$  adsorption as a function of gas pressure. An initial anisotropic expansion of each

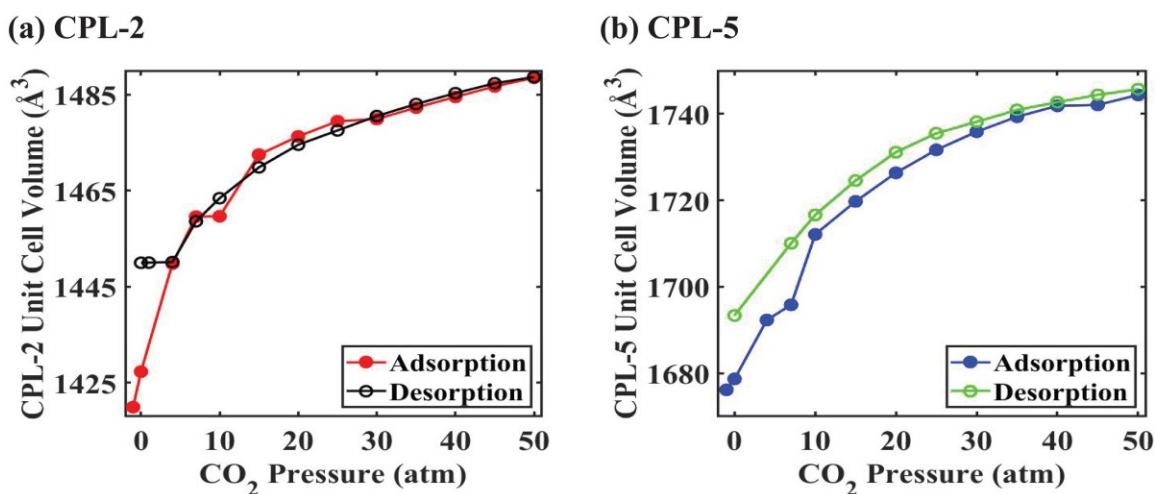


Figure 11. Unit cell volume as a function of  $\text{CO}_2$  pressure for (a) CPL-2 and (b) CPL-5 during a single adsorption-desorption cycle. The first point of the adsorption process represents the activated structures in 0 atm He.

initial unit cell is observed as the CO<sub>2</sub> gas pressure is varied. Figures 11(a) and 11(b) show the variation in the unit-cell volume of CPL-2 and CPL-5 as a function of CO<sub>2</sub> gas pressure. This lattice distortion is characteristic of a shape-responsive behavior displayed by CPL compounds in CO<sub>2</sub> gas environments. Therefore, preferential adsorption interactions on the framework internal pore surface are facilitated by the widening of the pore gallery size.

The lattice parameter  $a$  displays a different behavior in each material. In CPL-5,  $a$  decreases with increasing CO<sub>2</sub> pressure, reaching a minimum value near to 25 atm. The rigidity of CPL-2 restricts the expansion of  $a$ . One plausible consequence of this behavior in CPL-2 is a more uniform surface potential that results in distortion pathways for  $b$ ,  $c$ , and  $\beta$  that produce adsorption with lower hysteresis than in CPL-5. The most prominent structural distortion within CPL-2 and CPL-5 unit cell is a twisting of the pillar ligands which results in a modification of  $\beta$  lattice parameter. From a geometric perspective, the pillars can be pictured as having a fixed length. The flexible pillar ligands thus must reorient to accommodate the new framework geometry and lattice parameters resulting from CO<sub>2</sub> adsorption. The twisting of the ligands can be determined from the structures determined from the Rietveld refinement analysis by measuring the change angle between the neutral layer containing the Cu node and members of the heterocyclic rings that compose the *pzdc* and *bpe/bpy* groups. As hypothesized, the evolution of this dihedral angle as a function of CO<sub>2</sub> adsorption is clearly correlated to the overall lattice distortion, as shown schematically in Fig. 12(b).

In CPL compounds, the distortion of the unit cell is possible because the coordination chemistry of the bonding between the Cu<sup>2+</sup> cation and the ligands allows flexibility in the ligand orientation with respect to the Cu<sup>2+</sup> coordination center.<sup>32</sup> This twisting distortion of *bpe* and *bpy* ligand groups has also been observed in a Zn-based flexible MOF with a structure similar to the

CPLs.<sup>33</sup> Flexible N-donor ligands have also been employed in the design of MOFs that effectively trap CO<sub>2</sub> adsorbate after the pore geometry is modified during an activation process by which water molecules are removed from the pore structure.<sup>34</sup> This elastic trapping effect is enabled by conformational changes in the flexible ligand which ultimately accompany significant modifications to the lattice parameters during CO<sub>2</sub> adsorption.

The rotation of the ligand groups in CPL-2 and CPL-5 accompanies changes in the angle  $\beta$  and the  $b$  and  $c$  lattice parameters during the adsorption-desorption cycle and ultimately accommodates growth in the pore volume.<sup>28</sup> The extent of ligand rotation is determined from the dihedral angle, which defines the angle between the plane containing the N and C atoms of the pyridyl ring and the plane containing the Cu node, an adjacent O, and the N member of the pyridyl ring. The atoms used to determine the dihedral angle are shown in the CPL-5 fragment in Fig. 12(a). The ligand twisting that leads to the variation in dihedral angle is demonstrated in Fig. 12(b), which shows *bpe* ligands of CPL-5 prominently distorting as the CO<sub>2</sub> gas pressure is varied. The dihedral angle of CPL-2, shown in Fig. 12(c) changes from 93.5° at 0 atm CO<sub>2</sub> to 107.9° at 50 atm CO<sub>2</sub>. The evolution of the angle in Fig. 12(c) indicates that the pyridyl ligands evolve in a complex free-energy landscape in which disorder has an important effect and which could, in principle exhibit multiple local minima near the low- and high-pressure configurations. Figure 12(d) shows the dihedral angle of CPL-5, which changes from 110.5° at 0 atm CO<sub>2</sub> to 146.3° at 50 atm CO<sub>2</sub>.

The diffraction data also provide insight into the reversibility of the lattice distortion during the adsorption and desorption of CO<sub>2</sub>. The CO<sub>2</sub>-induced structural changes in CPL-2 exhibit an incomplete return to the initial 0 atm structural state after depressurization. The structural response to CO<sub>2</sub> adsorption thus differs from the full reversibility observed in the volumetric adsorption measurements.<sup>31</sup> In comparison, the structural relaxation of CPL-5 following depressurization

proceeds completely back to its 0 atm structure. The greater extent of structural relaxation after desorption in CPL-5 is likely due to a lower heat of desorption in CPL-5 than in CPL-2.<sup>24</sup>

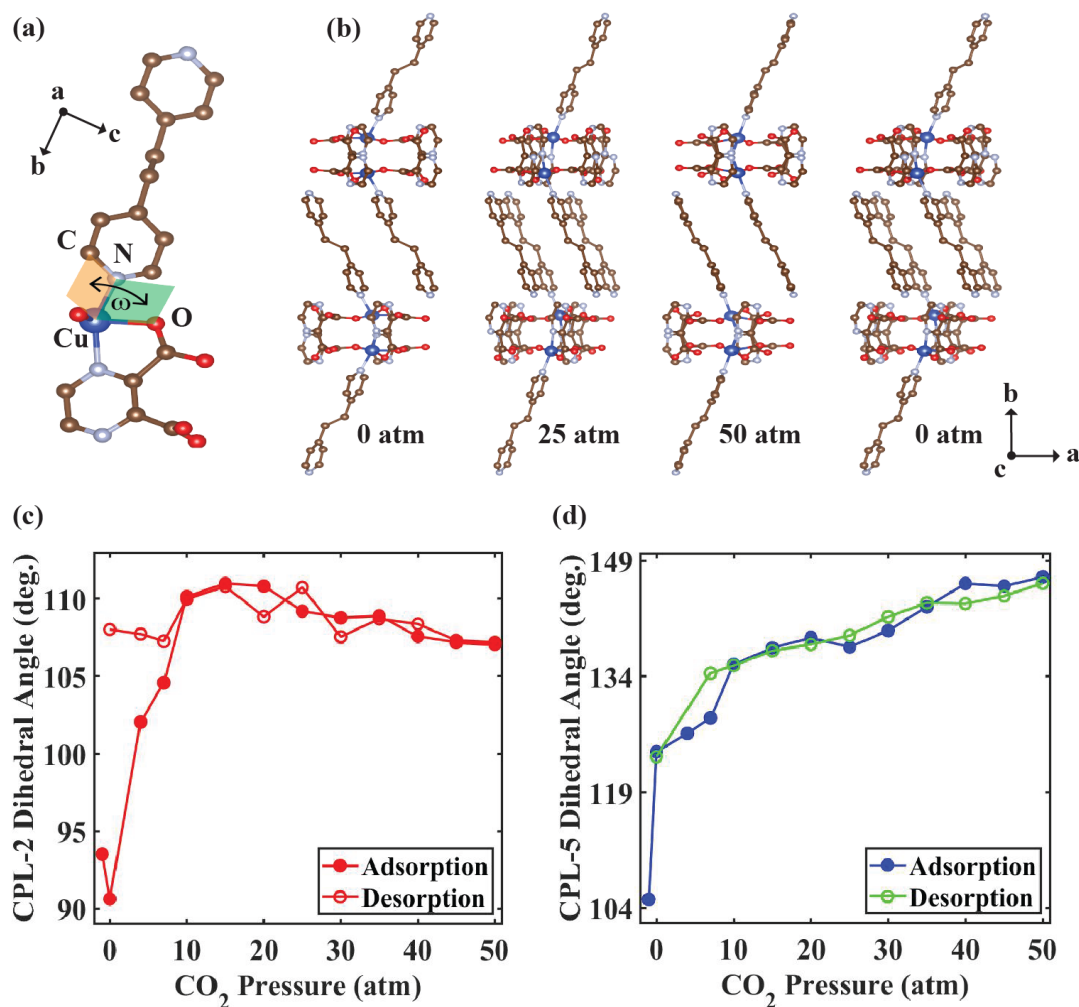


Figure 12. (a) Fragment of CPL-5 with the dihedral angle,  $\omega$ , defined between the orange plane containing the C, N, and Cu atoms and the green plane containing the N, Cu, and O atoms. (b) Schematic of the ligand rotation as a function of CO<sub>2</sub> pressure at 0 atm, 25 atm, and after depressurization to 0 atm. Dihedral angle of CPL-2 (c) and CPL-5 (d) ligands as function of CO<sub>2</sub> pressure.

The volumetric isotherms of CPL-2 and CPL-5, shown in Fig. 4, both exhibit hysteresis in the adsorption and desorption of CO<sub>2</sub>. The distinct adsorption and desorption pathways seen in the isotherms in Fig. 5 may result from modification of the pore surface during adsorption. The hysteresis observed in this study is an order of magnitude smaller than reported in previous studies

at CO<sub>2</sub> pressure up to 7 atm.<sup>29</sup> The adsorption-desorption hysteresis in the structure of CPL-2 is likely due to interactions between the adsorbate and host structure in which occupancy of the guest molecules within the pores persists at atmospheric conditions. This hysteretic adsorption behavior could also explain the difference in the magnitude of the lattice parameters between the initial and final structure. Furthermore, residual CO<sub>2</sub> molecules remaining adsorbed during the depressurization stage could be responsible for the observed path difference between the adsorption and desorption stages.

The structural analyses and the adsorption isotherms together indicate that the hysteretic behavior depends on the maximum degree of structural expansion, which, in turn, depends on the maximum CO<sub>2</sub> pressure reached during the adsorption process. The hysteresis also suggests that the path of the return to the original structure differs during the desorption stage due to an evolution of the CPL surfaces that occurs during the adsorption stage when CO<sub>2</sub> adsorbs at the active sites. Possible origins of the hysteresis in CPL-2 include previously observed adsorbate-adsorbate interactions.<sup>24</sup> A second origin could be related to new adsorbate accessibility near the adsorption sites during the adsorption stage as the structure is expanding.

The structures obtained from the powder X-ray diffraction study also provides insight into the location of adsorbed CO<sub>2</sub> molecules within the CPL unit cell. The sites of the CO<sub>2</sub> molecules are important in understanding the interactions between the host framework and adsorbate that produce the structural distortions and determining the adsorption and desorption mechanisms. The CO<sub>2</sub> adsorption at 50 atm corresponded to the addition of 3 molecules of CO<sub>2</sub> per CPL formula unit, which results in the addition of charge density that was not accounted for in the initial activated structure and which results in the observation of a spatially localized residual charge density in the Rietveld analysis. The residual electron density can be accounted for by considering

the accumulation of disordered CO<sub>2</sub> molecules dispersed throughout the pores of the structure of the CPLs during adsorption. The residual electron density as a function of fractional position within the unit cell,  $\rho(\mathbf{X})$ , was determined from the refined structures at each CO<sub>2</sub> pressure step using Eqn. 3.

Computational studies indicate that there are two regions of strong CO<sub>2</sub>-host interactions within CPL-2 and CPL-5 frameworks.<sup>35</sup> These regions are both located: (i) at the carboxylate groups and (ii) at aromatic rings of the ligands. The Fourier difference meshes in Fig. 9 reveal that residual electron density due to CO<sub>2</sub> is distributed throughout the pore gallery in the vicinity of the pillar ligands and carboxylate groups.

Electron density distributions for 0 atm CO<sub>2</sub> after depressurization in CPL-2 and CPL-5 are also shown in Fig. 9. The residual electron density after reducing the CO<sub>2</sub> pressure to 0 atm indicates that residual CO<sub>2</sub> is trapped or weakly adsorbed in the CPL frameworks after depressurization. More CO<sub>2</sub> remains in the CPL-2 framework than the CPL-5 framework after depressurization, clearly seen in the 0 atm CO<sub>2</sub> Fourier difference meshes which show significant contour in the CPL-2 pore gallery compared to the CPL-5 pore gallery. The structural observation that a higher concentration of CO<sub>2</sub> remains in CPL-2 after depressurization agrees with the hysteresis observed in the lattice distortions and adsorption isotherms.

## 5. Experimental

### 5.1 Synthesis

CPL-2 and CPL-5 were synthesized at room temperature following procedures described elsewhere.<sup>21, 23, 29, 32</sup> Common reagents used for each CPL compound were 2,3-pyazinedicarboxylic acid (H<sub>2</sub>pzdc, 97% purity) and copper(II) perchlorate hexahydrate

( $\text{Cu}(\text{ClO}_4)_2 \cdot 6\text{H}_2\text{O}$ , 98% purity). Other reagents used were 4,4'-bipyridine (*bpy*) and 1,2-di-(4-pyridyl)-ethylene (*bpe*), which comprised the pillar ligands for CPL-2 and CPL-5, respectively. One mmol of  $\text{H}_2\text{pzdc}$  (0.1681g) and 0.5 mmol of the desired ligand were dissolved in a solution prepared by mixing 1:1 NaOH 0.04M and ethanol. The mixture was added drop-wise to a second solution consisting of  $\text{CuClO}_4 \cdot 6\text{H}_2\text{O}$  (0.37g) and water while under continuous agitation. The final blend was stirred for 24 h, filtered under vacuum, and washed with methanol and deionized water repeatedly. The residual methanol was removed by heating the solid overnight at 90°C in air.

### 5.2 *In situ* synchrotron x-ray experiments

Synchrotron X-ray powder diffraction experiments were conducted at station 17-BM of the Advanced Photon Source of Argonne National Laboratory using an X-ray wavelength of 0.72768 Å. X-ray powder diffraction patterns were recorded using an amorphous-Si flat panel detector (Perkin Elmer, Inc.) positioned at a distance of 0.5 m from the sample. The angular range in  $2\theta$  was 2-20°. Powder specimens were loaded into cylindrical quartz capillaries with a 1 mm diameter. Glass wool was packed into both ends of the capillary to reduce sample displacement during gas flow and a thin-wire type-K thermocouple was inserted into the capillary near the powder to monitor the temperature. The X-ray beam probed a region immediately adjacent to the thermocouple to ensure accurate temperature measurement. The capillaries were mounted on a sample holder equipped with two resistive heaters with a 5-mm gap between the heaters and the walls of the capillary tube. The capillary was attached to the sample holder with gas fittings. The He and  $\text{CO}_2$  gas were supplied at 99.999% purity.

The sample activation procedure consisted of heating the CPL powder in helium gas while collecting diffraction data. After flowing He at atmospheric pressure and 30 min at 100-106 °C,

the gas atmosphere was switched to CO<sub>2</sub>. A syringe pump was used to deliver gas to the sample cell at a pressure ramp rate of 1 atm/s. Diffraction data were acquired after allowing the gas pressure to equilibrate for at least 3 min at each step in the CO<sub>2</sub> pressure. The diffraction patterns were constructed by summing the intensities of ten exposures with an acquisition time of 3 s per exposure. Control experiments were conducted for CPL-2 and CPL-5 using N<sub>2</sub>.

### 5.3 Structure refinement

The Rietveld refinement was conducted using the GSAS II software package.<sup>36</sup> The refinement residuals used in this work were based on the weighted profile R-factor, defined as

$$R_{wp} = \sqrt{\sum_i w_i (y_{c,i} - y_{o,i})^2 / \sum_i w_i (y_{o,i})^2} \quad \text{and} \quad \text{the expected R-factor, } R_{exp} =$$

$\sqrt{N / \sum_i w_i (y_{o,i})^2}$ .<sup>37</sup> Several intensity maxima in the CPL-2 diffraction pattern originated from an impurity phase present in the sample and were thus omitted from the refinement. The omitted angular ranges appear as gaps in the diffraction patterns in Fig. 5.

Values for isotropic thermal ellipsoids (Uiso) for each atom in the CPL-2 and CPL-5 structures were selected from previously reported structures. Attempts to refine the values of Uiso resulted in negative values, which can be indicative of structural disorder that, in this case, likely arises from the incorporation of a disordered adsorbate.<sup>38</sup> Therefore, Uiso was held fixed during the structure refinement.

The residual electron density in the refined structures exhibits sharp peaks at 13.6 Å<sup>-3</sup> and 15.6 Å<sup>-3</sup> for CPL-2 and CPL-5, respectively. These peaks are located near the Cu nodes and arise from the displacement of the Cu ion during CO<sub>2</sub> adsorption from the fractional atomic coordinates of the initial structure. These peaks persist through the parametric refinements of CPL-2 and CPL-

5 because changes to the fractional atomic positions for each crystal are evaluated with respect to the structure obtained from the previous CO<sub>2</sub> pressure step.

High-pressure CO<sub>2</sub> adsorption isotherms were measured using a Particulate Systems HPVA-II 100 at (Micromeritics Instrument Corporation (Georgia, US)). This instrument employed a static volumetric system, connected to a high vacuum source. Between 250-450 mg of each CPL material was used for these tests. The samples were activated for adsorption measurements by heating to 373 K under vacuum for 4 hours. The volumetric adsorption was measured for the same CO<sub>2</sub> gas pressures as the accompanying X-ray study, with two additional pressure steps in the 0 - 10 atm range. A wait time of at least 10 min was implemented after equilibrium at each adsorption/desorption pressure step before continuing the experiment. This equilibration time was the maximum allowable due to instrument usage logistics. Sample temperature was maintained at 25 °C using a recirculating water bath.

#### 5.4 Thermodynamic calculations

Heats of adsorption and desorption profiles for CO<sub>2</sub> loading onto the CPL materials were estimated using the following expression<sup>39</sup>

$$-\Delta H = \Delta H_{vap} + \beta_{DA} E \left( \ln \frac{q_0}{q} \right)^{\frac{1}{n}} + \frac{(\beta_{DA} E) \delta T}{n} \left( \ln \frac{q_0}{q} \right)^{-\left( \frac{n-1}{n} \right)} \quad \text{Equation 4}$$

which results after a combination of the Dubinin-Astakhov isotherm model (applied to either the adsorption or desorption legs)

$$q = q_0 \exp \left[ - (C \ln(P_0 / P))^n \right] \quad \text{Equation 5}$$

$$C = \frac{RT}{\beta_{DA} E}$$

with the Clausius-Clapeyron equation

$$-\Delta H = R \left. \frac{d \ln P}{d(1/T)} \right|_{@ \text{ constant loading}} \quad \text{Equation 6}$$

where  $\Delta H_{vap}$  is the adsorbate heat of vaporization,  $q$  is the equilibrium desorption amount,  $q_0$  is the adsorbate loading amount at or near saturation,  $T$  is the temperature during the desorption tests,  $\beta$  is the affinity coefficient of the adsorbate,  $E$  is the energy of desorption,  $P$  is the gas pressure,  $P_0$  is the adsorbate vapor pressure,  $n$  is an heterogeneity coefficient,  $\delta$  is a thermal expansion coefficient for the adsorbate (assumed as  $0.0024 \text{ K}^{-1}$ ),<sup>40</sup> and  $R$  is the ideal gas constant.

## 6. Conclusion

CO<sub>2</sub> adsorption at pressures up to 50 atm induces structural changes in CPL-2 and CPL-5. CPL-2 exhibits greater lattice distortion in all lattice parameters corresponding to a greater enhancement of pore volume, and therefore CO<sub>2</sub> adsorption capacity. CPL-2 exhibits greater hysteresis upon desorption than CPL-5, evident in the residual electron density within the unit cell pore gallery after depressurization.

CPL-5 shows a significant degree of hysteresis in its adsorption-desorption behavior as compared to CPL-2. CPL-5 also exhibits a greater magnitude of the ligand twist distortion responsible for pore volume enhancement. However, CPL-5 shows significantly greater CO<sub>2</sub> uptake than predictions based on pore volume despite the greater framework rigidity compared to CPL-2. The smaller hysteresis in CPL-5 suggests the large lattice distortions in CPL-2 result in greater retention of CO<sub>2</sub> at atmospheric pressure after an adsorption cycle.

Residual electron density contours corresponding to adsorbed CO<sub>2</sub> within the CPL galleries shows a remnant concentration of CO<sub>2</sub> within the CPL-2 pore gallery. This residual electron density is observed near the *bpy* groups in CPL-2 and the *bpe* groups in CPL-5. The interaction

sites for CO<sub>2</sub> adsorption on the host frameworks are consistent with those predicted by DFT calculations.

These results bring new insight to the shape-responsive behavior of MOFs in high-pressure CO<sub>2</sub> environments that can be applied in the design of MOFs and in potential technological applications. On a broader scientific scale, the experimental and analysis techniques applied here could be extended to new studies of storage materials in extreme environments, particularly when probing the interactions between crystalline porous materials and intrinsically disordered gas phases seen extensively in separation and storage systems.

### **Acknowledgements**

Partial funding for this work was provided by the National Science Foundation (NSF) Partnership for Research and Education in Materials (PREM) Award DMR-1827894. PGE and SDM acknowledge support from the University of Wisconsin Materials Research Science and Engineering Center (DMR-1720415). This research used resources of the Advanced Photon Source, a U.S. Department of Energy (DOE) Office of Science User Facility operated for the DOE Office of Science by Argonne National Laboratory under Contract No. DE-AC02-06CH11357.

**Corresponding Author**

\*sdmarks2@wisc.edu

**Conflicts of Interest**

The authors declare no conflicts of interest.

**Author Contributions**

This manuscript was written through contributions of all authors. SM, AY, PE, and AH conducted the experiment at the Advanced Photon Source. SM, KR, RP, PE, and AH carried out data analysis and writing. JE conducted the adsorption isotherm measurements.

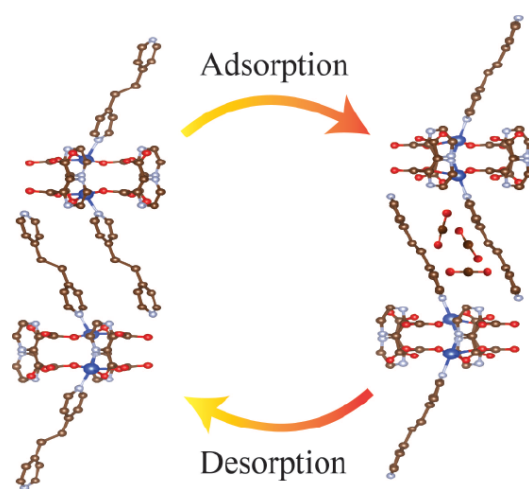
† Original crystallographic data were obtained from Cambridge Crystallographic Data Centre (CCDC). CCDC 781721 for CPL-2 and CCDC 1402666 for CPL-5.

## References

1. S. Kitagawa, *Chem. Soc. Rev.*, 2014, **43**, 5415-5418.
2. J.-R. Li, J. Sculley and H.-C. Zhou, *Chem. Rev.*, 2012, **112**, 869-932.
3. D. M. D'Alessandro, B. Smit and J. R. Long, *Angew. Chem. Int. Ed.*, 2010, **49**, 6058-6082.
4. C.-H. Yu, C.-H. Huang and C.-S. Tan, *Aerosol Air Qual. Res.*, 2012, **12**, 745-769.
5. S. D. Kenarsari, D. Yang, G. Jiang, S. Zhang, J. Wang, A. G. Russell, Q. Wei and M. Fan, *RSC Advances*, 2013, **3**, 22739-22773.
6. M. T. Ho, G. W. Allinson and D. E. Wiley, *Ind. Eng. Chem. Res.*, 2008, **47**, 4883-4890.
7. F. A. A. Paz, J. Klinowski, S. M. Vilela, J. P. Tome, J. A. Cavaleiro and J. Rocha, *Chem. Soc. Rev.*, 2012, **41**, 1088-1110.
8. M. Pardakhti, E. Moharreri, D. Wanik, S. L. Suib and R. Srivastava, *ACS Comb. Sci.*, 2017, **19**, 640-645.
9. S. Kitagawa, R. Kitaura and S. i. Noro, *Angew. Chem. Int. Ed.*, 2004, **43**, 2334-2375.
10. J.-R. Li, R. J. Kuppler and H.-C. Zhou, *Chem. Soc. Rev.*, 2009, **38**, 1477-1504.
11. L. Huang, H. Wang, J. Chen, Z. Wang, J. Sun, D. Zhao and Y. Yan, *Microporous Mesoporous Mater.*, 2003, **58**, 105-114.
12. H.-C. Zhou, J. R. Long and O. M. Yaghi, *Chem. Rev.*, 2012, **112**, 673-674.
13. R. Kitaura, K. Fujimoto, S. i. Noro, M. Kondo and S. Kitagawa, *Angew. Chem.*, 2002, **114**, 141-143.
14. Z.-J. Lin, J. Lü, M. Hong and R. Cao, *Chem. Soc. Rev.*, 2014, **43**, 5867-5895.
15. M. Alhamami, H. Doan and C.-H. Cheng, *Materials*, 2014, **7**, 3198-3250.
16. D. N. Dybtsev, H. Chun and K. Kim, *Angew. Chem.*, 2004, **116**, 5143-5146.

17. G. Férey and C. Serre, *Chem. Soc. Rev.*, 2009, **38**, 1380-1399.
18. H. S. Choi and M. P. Suh, *Angew. Chem. Int. Ed.*, 2009, **48**, 6865-6869.
19. P. K. Thallapally, J. Tian, M. Radha Kishan, C. A. Fernandez, S. J. Dalgarno, P. B. McGrail, J. E. Warren and J. L. Atwood, *J. Am. Chem. Soc.*, 2008, **130**, 16842-16843.
20. J.-R. Li, Y. Ma, M. C. McCarthy, J. Sculley, J. Yu, H.-K. Jeong, P. B. Balbuena and H.-C. Zhou, *Coord. Chem. Rev.*, 2011, **255**, 1791-1823.
21. R. Matsuda, R. Kitaura, S. Kitagawa, Y. Kubota, T. C. Kobayashi, S. Horike and M. Takata, *J. Am. Chem. Soc.*, 2004, **126**, 14063-14070.
22. H. Sakamoto, R. Kitaura, R. Matsuda, S. Kitagawa, Y. Kubota and M. Takata, *Chem. Lett.*, 2010, **39**, 218-219.
23. O. J. García-Ricard, J. C. Silva-Martínez and A. J. Hernández-Maldonado, *Dalton Trans.*, 2012, **41**, 8922-8930.
24. H. Chen, K. Riascos-Rodríguez, M. E. Marcano-González and A. J. Hernández-Maldonado, *Chem. Eng. J.*, 2016, **283**, 806-815.
25. O. J. García-Ricard and A. J. Hernández-Maldonado, *J. Phys. Chem. C*, 2010, **114**, 1827-1834.
26. O. J. García-Ricard, R. Fu and A. J. Hernández-Maldonado, *J. Phys. Chem. C*, 2011, **115**, 3595-3601.
27. O. J. García-Ricard, P. Meza-Morales, J. C. Silva-Martínez, M. C. Curet-Arana, J. A. Hogan and A. J. Hernández-Maldonado, *Microporous Mesoporous Mater.*, 2013, **177**, 54-58.
28. P. J. Meza-Morales, D. A. Gómez-Gualdrón, R. R. Arrieta-Perez, A. J. Hernández-Maldonado, R. Q. Snurr and M. C. Curet-Arana, *Dalton Trans.*, 2016, **45**, 17168-17178.

29. K. Riascos-Rodríguez, A. J. Schroeder, M. R. Arend, P. G. Evans and A. J. Hernández-Maldonado, *Dalton Trans.*, 2014, **43**, 10877-10884.
30. A. L. Spek, *Acta Crystallogr. C Struct. Chem.*, 2015, **71**, 9-18.
31. M. L. Connolly, *Science*, 1983, **221**, 709-713.
32. S. Kitagawa and R. Matsuda, *Coordination Chemistry Reviews*, 2007, **251**, 2490-2509.
33. N. Nijem, P. Thissen, Y. Yao, R. C. Longo, K. Roodenko, H. Wu, Y. Zhao, K. Cho, J. Li and D. C. Langreth, *J. Am. Chem. Soc.*, 2011, **133**, 12849-12857.
34. M. Wriedt, J. P. Sculley, A. A. Yakovenko, Y. Ma, G. J. Halder, P. B. Balbuena and H. C. Zhou, *Angewandte Chemie*, 2012, **124**, 9942-9946.
35. P. J. Meza-Morales, A. Santana-Vargas and M. C. Curet-Arana, *Adsorption*, 2015, **21**, 533-546.
36. B. H. Toby and R. B. Von Dreele, *J. Appl. Cryst.*, 2013, **46**, 544-549.
37. B. H. Toby, *Powder Diffr.*, 2006, **21**, 67-70.
38. P. Jones, *Chemical Society Reviews*, 1984, **13**, 157-172.
39. D. D. Do, *Adsorption Analysis: Equilibria and Kinetics*, Imperial College Press, London, 1998.
40. K. A. M. Gasem, Z. Pan, S. Mohammad and R. L. Robinson, in *Carbon Dioxide Sequestration in Geological Media: State of the Science*, eds. M. Grobe, J. C. Pashin and R. L. Dodge, American Association of Petroleum Geologist, US, 2010.

**Marks *et al.* Table of Contents Figure**

*Table of Contents Figure: Schematic depiction of the CO<sub>2</sub> adsorption-induced lattice distortion and ligand rotation in CPL-5.*